Mapping cropping intensity in China using time series Landsat and Sentinel-2 images and Google Earth Engine

Luo Liu[a], Xiangming Xiao[b,*], Yuanwei Qin[b], Jie Wang[b], Xinliang Xu[c], Yueming Hu[a,**], Zhi Qiao[d]

[a] Guangdong Province Key Laboratory for Land Use and Consolidation, South China Agricultural University, Guangzhou 510642, China
[b] Department of Microbiology and Plant Biology, University of Oklahoma, Norman, OK 73019, USA
[c] State Key Laboratory of Resources and Environmental Information Systems, Institute of Geographical Sciences and Natural Resources Research, Chinese Academy of Sciences, Beijing 100101, China
[d] Key Laboratory of Indoor Air Environment Quality Control, School of Environmental Science and Engineering, Tianjin University, Tianjin 300350, China

ARTICLE INFO

ABSTRACT

Cropping intensity has undergone dramatic changes worldwide due to the effects of climate changes and human management activities. Cropping intensity is an important factor contributing to crop production and food security at local, regional and national scales, and is a critical input data variable for many global climate, land surface, and crop models. To generate annual cropping intensity maps at large scales, Moderate Resolution Imaging Spectroradiometer (MODIS) images at 500-m or 250-m spatial resolution have problems with mixed land cover types within a pixel (mixed pixel), and Landsat images at 30-m spatial resolution suffer from low temporal resolution (16-day). To overcome these limitations, we developed a straightforward and efficient pixel- and phenology-based algorithm to generate annual cropping intensity maps over large spatial domains at high spatial resolution by integrating Landsat-8 and Sentinel-2 time series image data for 2016–2018 using the Google Earth Engine (GEE) platform. In this pilot study, we report annual cropping intensity maps for 2017 at 30-m spatial resolution over seven study areas selected according to agro-climatic zones in China. Based on field-scale sample data, the annual cropping intensity maps for the study areas had overall accuracy rates of 89–99%, with Kappa coefficients of 0.76–0.91. The overall accuracy of the annual cropping intensity maps was 93%, with a Kappa coefficient of 0.84. These cropping intensity maps can also be used to enable identification of various crop types from phenological information extracted from the growth cycle of each crop. These algorithms can be readily applied to other regions in China to generate annual cropping intensity maps and quantify inter-annual cropping intensity variations at the national scale with a greatly improved accuracy.

1. Introduction

Due to the combined influences of global climate change, human activities and urbanization, cropping intensity has undergone dramatic changes worldwide. Cropland refers to all agricultural land, including permanently cultivated land, newly cultivated land, fallow land, and land in a grassland-farming rotation (Liu et al., 2005). Increasing cropping intensity (one to three crops per year) is one of the most effective ways to increase grain yields from limited cropland (Liu et al., 2013). Cropping intensity is not only an important factor contributing to crop production and food security at local and national scales (Iizumi and Ramankutty, 2015; USDA, 1994; Wu et al., 2018), but also is tightly linked to ecosystem and human health (Wu et al., 2014; Zhang et al., 2014). Cropping intensity data can greatly improve food production assessments and predictions and therefore represent a critical input layer for many global climate, land surface, and crop models (Belcher et al., 2004; Dietrich et al., 2012; Meylan et al., 2013).

Several remote sensing approaches have been developed during recent decades to identify cropping intensity at moderate spatial resolution (Biradar and Xiao, 2011; Quarmby et al., 1992). Many studies have generated annual cropping intensity maps by analyzing crop phenological cycles within a single year using high-temporal-resolution vegetation index (VI) data, including the enhanced vegetation index (EVI) and normalized difference vegetation index (NDVI), which are
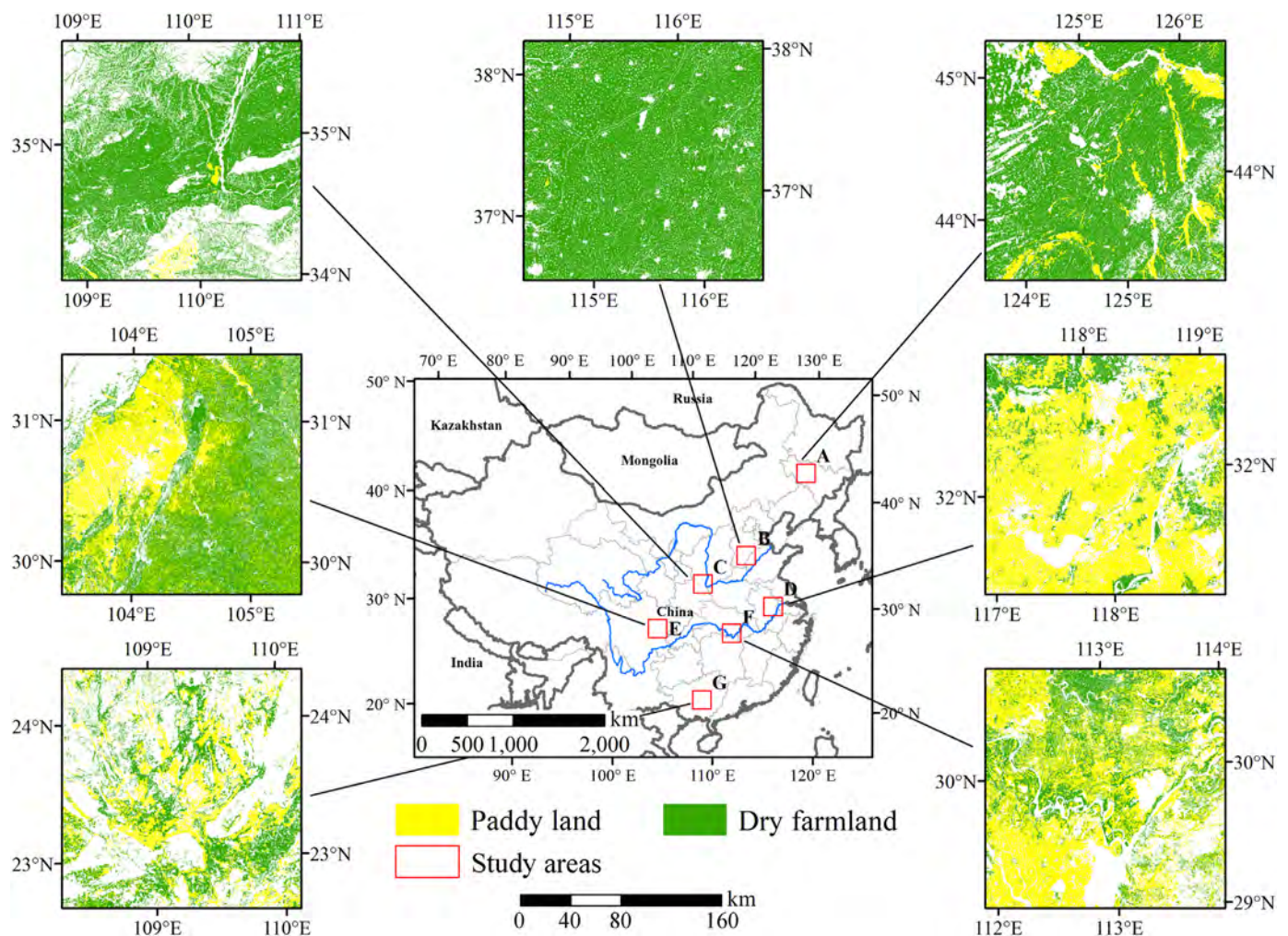

Fig. 1. Locations and cropland types of the seven study areas in China. A is located on the Northeast China Plain (123.5296˚E - 126.5111˚E, 43.1943˚N -45.2910˚N); B on the North China Plain (114.2911˚E - 116.8191˚E, 36.3114˚N - 38.2581˚N); C on Guanzhong Plain (108.7615˚E - 111.0956˚E, 33.9207˚N - 35.7769˚N); D on Tai Lake Pain (116.8555˚E - 119.2689˚E, 31.0419˚N - 33.0357˚N); E on the Sichuan Basin (103.3805˚E - 105.5170˚E, 29.7363˚N - 31.5264˚N); F on Dongting Lake Plain (111.8394˚E - 114.0955˚E, 28.9197˚N - 30.8397˚N); and G on the Central Guangxi Plain (108.2154˚E - 110.2461˚E, 22.5774˚N - 24.4670˚N).

typically calculated from Moderate Resolution Imaging Spectro-radiometer (MODIS) images at 500-m and 250-m spatial resolutions (Galford et al., 2008; Sakamoto et al., 2005; Wardlow et al., 2007). Phenology has been used to quantify cropping intensity by counting the number of VI peaks and troughs within a year (Biradar and Xiao, 2011). Annual cropping intensity maps have been derived from MODIS data based on a peak detection method with reference to agro-meteorological observations (Yan et al., 2014). Annual crop intensity maps of mainland China at 500-m spatial resolution were developed for 2005–2012 using an iterative moving-window method and evaluated using visually interpreted time series data (Li et al., 2014). Another recent study constructed the annual cropping intensity maps of Asia for 2009–2012 using MODIS images (Gray et al., 2014). However, MODIS pixels frequently include a mixture of different crop types due to the limitation of their moderate spatial resolution. Croplands often vary in field size, particularly in hilly regions, where crops are typically smaller than one MODIS pixel, which can result in sub-pixel heterogeneity in crop type and intensity.

To overcome MODIS sub-pixel heterogeneity, it is necessary to use remote sensing images with higher spatial resolution, such as Landsat images (30-m resolution) to determine cropping intensity (Jain et al., 2013; Lenney et al., 1996). Some studies have applied the Landsat threshold method to estimate cropping intensity using season-specific NDVI thresholds to distinguish cropped and uncropped land in a given

season (Fan et al., 2014; Lenney et al., 1996). One study found that the Landsat threshold method was more accurate than the MODIS time series peak method for mapping the cropping intensity of smallholder farms (< 2 ha) (Jain et al., 2013). However, the Landsat threshold method requires at least one good-quality Landsat image during each of the growing seasons, but the availability of good-quality Landsat data is much lower than that of MODIS data. On average, only 10–15 good-quality global Landsat datasets are obtained each year; only 5–8 are obtained in pluvial regions due to low temporal resolution and heavy cloud cover (Li and Roy, 2017; Zhu and Woodcock, 2014). In some years and regions, no good-quality Landsat data can be obtained during an entire cropping cycle due to extensive and frequent cloud cover and shadow. Therefore, the data required to identify cropping intensity are not guaranteed in most agricultural regions worldwide. Although Landsat offers improved spatial resolution over MODIS, it may not be able to provide the necessary temporal resolution to identify cropping intensity.

Sentinel-2 is an Earth observation mission by the European Union Copernicus Program that systematically acquires optical imagery at high spatial resolution. The mission is a constellation of two satellites that were launched in June 2015 (Sentinel-2a) and March 2017 (Sentinel-2b). Sentinel-2 sensors have spatial resolutions of 10, 20, and 60 m, and include 13 bands in the visible, near infrared, and shortwave infrared part of the spectrum. Together, the Sentinel-2 satellites have a

high revisit frequency of 5 days. Sentinel-2 data provide spectral information and spatial resolution similar to those of Landsat data. Integration of Landsat and Sentinel-2 data would significantly improve the temporal resolution of observations (Li and Roy, 2017) and could provide an effective solution to the problems of the low availability of Landsat data and the low spatial resolution MODIS in mapping cropping intensity. Thus, there is a need to assess the potential of such data integration and its application to crop phenological cycle identification for mapping cropping intensity over large areas, to complement data products already derived from time series MODIS images (Griffiths et al., 2019; Jain et al., 2013; Xiong et al., 2017a; Xiong et al., 2017b).

In this study, we developed a straightforward algorithm to efficiently integrate Landsat and Sentinel-2 time series data and apply the resulting data to mapping cropping intensity information at large scales. We selected seven study areas across China to assess the results using field-scale sample data. The main objective of this study was to integrate time series data from multiple remote sensors and extract cropping intensity with high precision and high spatial resolution over large scale domains.

2. Materials and methods

2.1. Study area

China has the largest multiple cropping areas in the world (Wu et al., 2018), with multiple cropping systems developed over a period exceeding 2000 years (Guo, 1986). In recent decades, nearly half of China's arable land has been devoted to multiple cropping systems (Yan et al., 2018a). To assess the accuracy and large-scale applicability of the improved algorithm proposed in this study, we selected seven study areas (A–G) representing all major grain-producing regions in China, each with an area of 200 km × 200 km, divided according to agro-climatic zones (Fig. 1), which are defined based on climate variables that influence crop growth and yield (Van Wart et al., 2013; Zuo, 1996). Three of the study areas (A, B and C) are in northern China; these sites experience mostly sunny days throughout the year and are covered mainly by large fields. The remaining four areas (D, E, F and G) are in southern China, have mostly cloudy and rainy weather year-round and are covered mainly by small-size cropland fields (Table 1).

2.2. Landsat and Sentinel-2 images and pre-processing

2.2.1. Image selection

To map cropping intensity in 2017, remote sensing data acquired by Landsat and Sentinel-2 between August 2016 and July 2018 were used, because cropping intensity in 2017 included winter crops (e.g., winter wheat and winter rapeseed) from 2016 to 2017 and 2017 to 2018. The Google Earth Engine (GEE) cloud computing platform (Gorelick et al., 2017) hosts both Sentinel-2 images (MSI) and Landsat images including Thematic Mapper (TM), Enhanced Thematic Mapper Plus (ETM+), and Operational Land Imager (OLI) images. At the time that we conducted our image analyses, all Sentinel-2 images in GEE were top-of-atmosphere reflectance (TOA) data, all Landsat 7/8 data were TOA data, and some Landsat data were surface reflectance (SR) data. We used

Table 2
Numbers of time series images available between August 2016 and July 2018.

	Landsat 7	Landsat 8	Sentinel-2	Total
A	292	379	2292	2963
B	254	298	2132	2684
C	230	302	1429	1961
D	190	189	1866	2245
E	171	243	1258	1672
F	115	145	1698	1958
G	126	218	1623	1967

Sentinel-2 and Landsat TOA data in this study (Table 2).

2.2.2. Image quality assessment

All bad-quality observations were identified, including cloud, cloud shadow, cirrus, and snow, as well as Landsat 7 ETM+ scan line corrector (SLC)-off gaps, which accounted for up to 22% of the pixels within an image (Arvidson et al., 2006). We used ETM+ metadata to identify SLC-off gaps in the images. The FMask algorithm (Foga et al., 2017; Zhu et al., 2015) was used to identify cloud, cloud shadow, cirrus, and snow/ice observations during ETM+, OLI and multispectral instrument (MSI) data processing.

We counted total observations and good-quality observations for the individual pixels in the seven study areas during the study period (8/2016–7/2018) (Fig. 2). Among the individual pixels, there were > 7 good-quality observations from ETM+ data, 23 from OLI data, and 81 from MSI data. There were much more MSI data than Landsat (ETM+ and OLI) data in terms of both total and good-quality observations. Notably, MSI data represented two times more data than the total of ETM+ and OLI data among good-quality observations over all study areas. Integrating ETM+, OLI, and MSI data resulted in > 114 observations for the study areas, such that a large amount of phenology information was extracted for cropping intensity determination.

The numbers of total and good-quality observations for individual pixels varied spatially during the study period (Fig. 3a-g, Fig. 4a-g). About 87.11%, 89.97%, 61.53%, 44.10%, 44.66%, 47.52%, and 73.34% of pixels had > 200 total observations in regions A–G, respectively (Fig. 3h). About 87.82%, 98.84%, 70.71%, 56.03%, 18.11%, 48.37%, and 13.24% of pixels had > 100 good-quality observations for regions A–G, respectively (Fig. 4h). The numbers of total and good-quality observations in northern China greatly exceeded those in southern China. The highest numbers of good-quality observations within a single pixel occurred in regions A and B, and the lowest numbers occurred in regions E and G. These results indicate that cropping intensity cannot be determined by counting growth cycles without the use of MSI data, and that the accuracy of this method may be much higher in northern China than in southern China.

2.2.3. Imagery harmonization

Due to subtle differences in band wavelengths among ETM+, OLI, and MSI images, remote sensing data must be unified to obtain comparable results. Therefore, we harmonized the ETM+ and MSI data to the standard of the OLI data. For ETM+ data, bands 3 (red), 4 (near

Table 1
A summary of elevation, topography, mean annual precipitation and air temperature, and major crops in each of seven study areas in China.

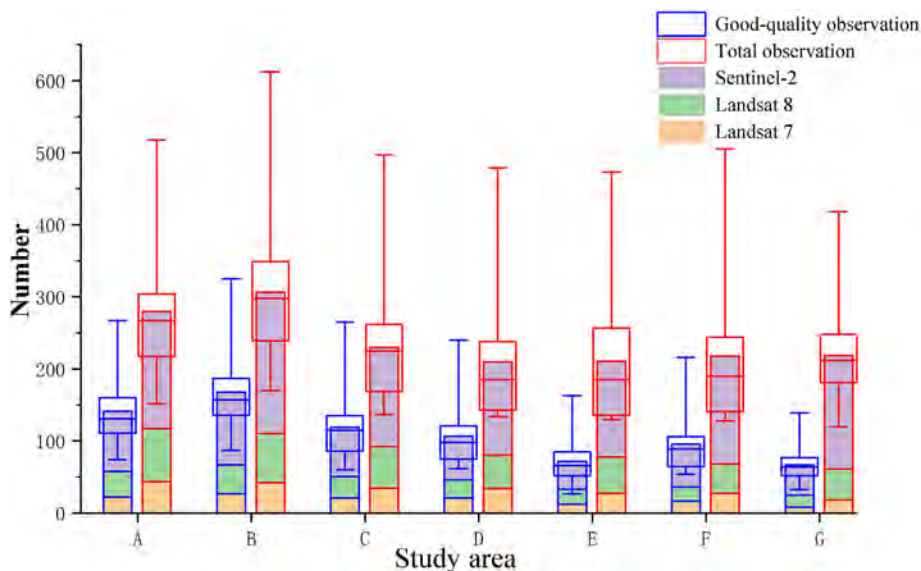| Region	Elevation (m)	Topography	Temperature (°C)	Precipitation (mm)	Main crops
A	< 200	Plain	5–7	350–700	Wheat, corn, soybeans, rice
B	< 50	Plain	11–15	500–700	Winter wheat, corn, soybeans
C	320–800	Plain, hills	12–14	550–660	Winter wheat, cotton
D	< 50	Plain	15–17	800–1100	Rice, rape
E	120–150	Plain, hills	20–22	1000–1600	Rice, sugar cane, rape
F	< 250	Plain	16–17	1100–1400	Rice, rape
G	120–150	Hills, plain	20–22	1000–1600	Rice, sugarcane, rape, vegetable

Fig. 2. Numbers of total observations and good-quality observations per pixel for various sensors (box represents the maximum, the third quartile, median, first quartile and minimum of all pixels in each study area).

infrared), and 5 (shortwave infrared) were transformed using the ordinary least squares regression coefficient (Roy et al., 2016). For MSI data, as the wavelength (near infrared) of band 8A matched that of OLI better, bands 4 (red), 8A (near infrared), and 11 (shortwave infrared) were selected and transformed using the ordinary least squares regression coefficient (Zhang et al., 2018). Due to differences in the spatial resolution of OLI and MSI data, MSI data were resampled to 30 m × 30 m using bicubic resampling.

2.2.4. Vegetation indices

NDVI (Tucker, 1979) and land surface water index (LSWI) (Xiao et al., 2005) values were calculated from TOA data, and the resultant times series VI data were used for phenology-based identification of cropping intensity. NDVI and LSWI were calculated from remote sensing data (Eqs. (1) and (2)).

$$NDVI = \frac{NIR - RED}{NIR + RED} \tag{1}$$

$$LSWI = \frac{NIR - SWIR}{NIR + SWIR} \tag{2}$$

Where RED is the TOA values of the red band (630–680 nm); NIR is the TOA values of the near infrared band (845–885 nm); and SWIR is the TOA values of the shortwave infrared band (1560–1660 nm).

2.2.5. Preparation of 10-day composite images

As remote sensing data from each sensor have a high degree of overlap and sidelap, it is possible to have two observations in many regions at different times on the same day. However, there are subtle differences between the vegetation indices. In addition, different sensors can cover the same region within a few days; the resulting images will also result in some differences among observed VI values. Therefore, to generate time series of equal lengths and intervals, we obtained 10-day composite NDVI values by calculating the maximum of all possible observed NDVI values during a 10-day period and a 10-day composite LSWI dataset by calculating the average of all possible
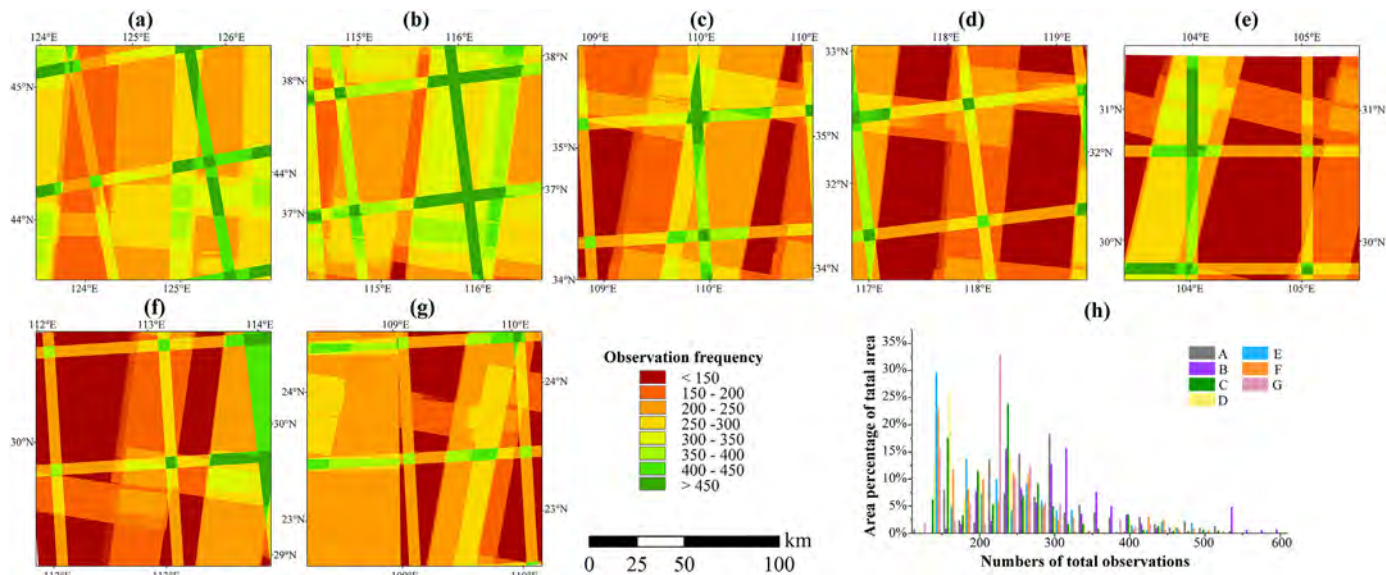

Fig. 3. Numbers of total observations for individual pixels during the study period. (a – g) show the spatial distributions of total observation numbers in each study area (A – G) respectively. (h) shows histograms of total observation numbers in all study areas.
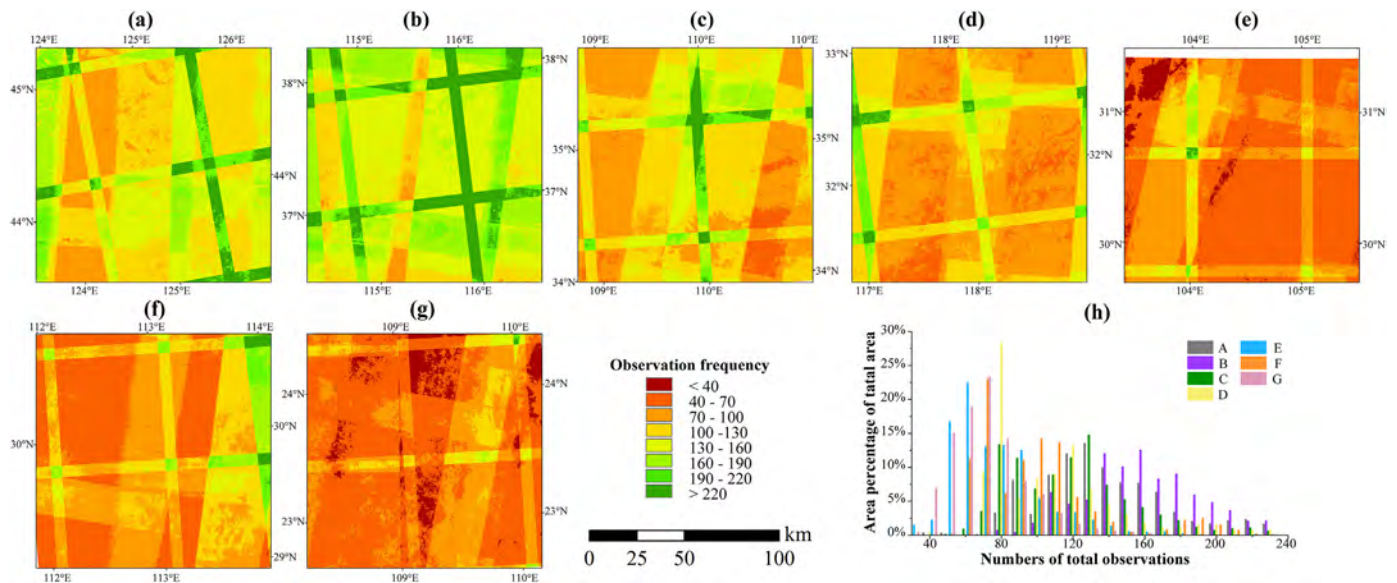
Fig. 4. Numbers of good-quality observations for individual pixels during the study period. (a – g) show the spatial distributions of good-quality observation numbers in each study area (A – G) respectively. (h) shows the histograms of good-quality observation numbers in all study areas.

observed LSWI values during a 10-day period (Running et al., 1995).

2.2.6. Gap filling and smoothing

Good-quality observations sometimes cannot be obtained in some regions during certain periods due to the influence of cloud, snow, or other factors. These gaps were filled by time-series linear interpolation based on good-quality observations before and after the time step (Kandasamy et al., 2013).

Uncertain factors such as aerosols and bidirectional reflectance can affect VI datasets by introducing various noise components. Although composite images and the removal of bad-quality observations are often applied in VI time series dataset processing, residual noise can remain in the dataset, impeding further analyses and resulting in the failure of cropping intensity determination. Therefore, such VI values should be smoothed to remove noise components before application. In theory, the NDVI curve should be continuous and smooth due to the narrow range of plant growth. To maximize the accuracy of NDVI values, we adopted the Savitzky–Golay filter to reconstruct these NDVI datasets, using a moving window of 9 observations and a filter order of 2, because the growth period of most crops exceeds 90 days (Fischer et al., 2002). Because LSWI varies under dry and wet conditions and LSWI smoothing was unnecessary, we did not reconstruct the LSWI dataset in this study.

2.3. Algorithms for identifying cropping intensity in a year for individual pixels

We developed an algorithm that uses the phenology of each pixel to identify and map cropping intensity, as shown in the workflow chart (Fig. 5).

2.3.1. Phenology and signature analyses of cropping intensity

We selected four typical sites representing single, double, and triple cropping intensities, using local questionnaires and Google Earth images. We created time series of NDVI and LSWI values at these sites to examine phenological characteristics of cropping intensity (Fig. 6). NDVI values gradually increased during the green-up stage, reaching a peak when crops matured, and then decreased from the senescence stage until harvest. Thus, cropping intensity could be determined from the number of crop growth cycles, as identified using the NDVI value profile by extracting the start and end periods of the plant growth cycle
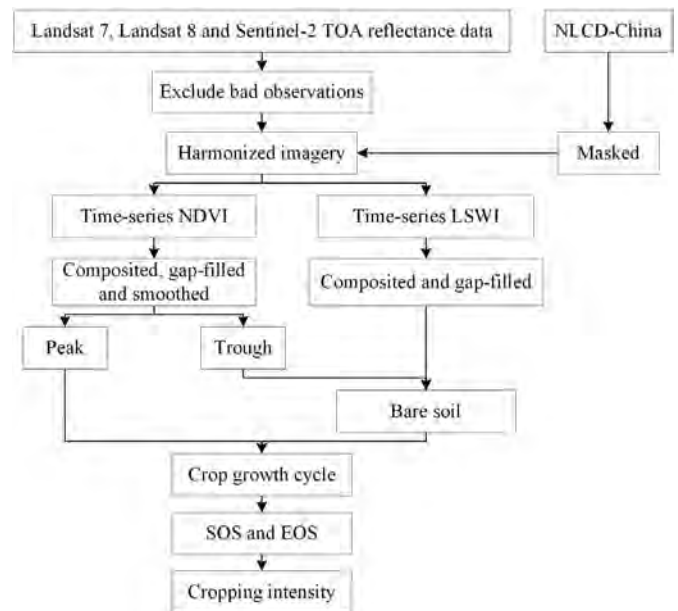

Fig. 5. Workflow schematic for phenology- and pixel-based cropping intensity mapping (top-of-atmosphere reflectance (TOA), National Land Cover Database (NLCD), normalized difference vegetation index (NDVI), land surface water index (LSWI), start of season (SOS), and end of season (EOS)).

from troughs in the NDVI time series.

Multiple NDVI waves can occur in winter crop growth cycles due to decreased NDVI during the vernalization period (Fig. 6b, November 2016 to June 2017) (Becker-Reshef et al., 2010). Some noise also remained in the NDVI temporal profile, which can result in multiple NDVI waves per crop growth cycle (Fig. 6d, October 2017 to February 2018). The start and end periods were defined as before the sowing period and after the harvest period, respectively, and were therefore characterized by bare soil. These periods were extracted by identifying bare soil during all troughs in the data. LSWI values are much lower for bare soil than for green vegetation, which makes them an important indicator for bare soil and for identifying the start and end periods of plant growth cycles (Boles et al., 2004; Chen et al., 2018; Dong et al., 2015). However, in some areas with early and late rice crops, the harvest of early
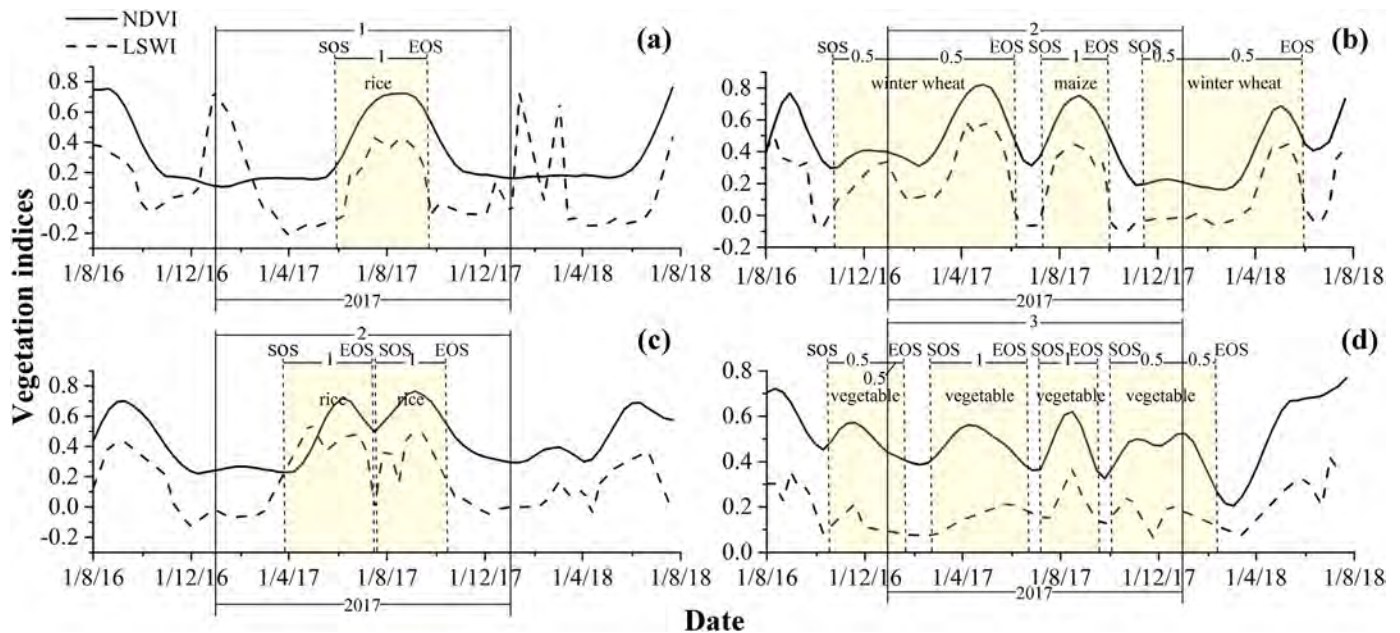
Fig. 6. Temporal profile of vegetation indices (NDVI and LSWI) for cropping intensity sample sites with (a) single cropping (124.7143°E, 43.6478°N), (b) double cropping (114.8321°E, 37.3673°N), (c) double cropping (113.2629°E, 29.1703°N), and (d) triple cropping (109.2024°E, 24.1904°N).

rice and transplanting of late rice usually occurs within a 2-week period between June and September (Fig. 6c, July in 2017), and LSWI values increase rapidly after late rice is transplanted. Therefore, bare soil between these two cropping periods may not be captured using LSWI values if no suitable observations are acquired, which makes NDVI values critical during this 2-week period. Therefore, another supplementary algorithm was applied to account for the short rice harvesting–transplanting period when it could not be identified.

Non-crop (e.g., weed) plants can grow before crop planting or after harvest (Fig. 6a, February to May 2017); their maximum NDVI values are typically much lower than those of crops. Therefore, the crop growth cycle can be identified using maximum NDVI values from the plant growth cycle.

The start and end of the growing season (SOS/EOS) of each crop growth cycle was extracted based on phenological characteristics and used to calculate cropping intensity.

2.3.2. Algorithm for crop intensity mapping

Step 1. A simple peak-finding method was used to identify all peaks and troughs in the NDVI time series data based on a moving window. If the NDVI value at a certain time was higher than those before and after that time, then it was defined as a peak. If an NDVI value at a certain time was lower than those before and after that time, then it was defined as a trough.

Step 2. During a trough period, bare soil was identified based on a dynamic threshold method, such that maximum and minimum LSWI values were calculated throughout the entire period. Recent studies indicated that in northern China, areas where LSWI values are < 0 was identified as bare soil (Biradar and Xiao, 2011; Dong et al., 2015), while in southern China, areas where LSWI value are < 0.2 can be identified as bare soil (Chen et al., 2018) due to higher soil moisture levels. Thus, the maximum LSWI threshold was set at 0.2 and the minimum LSWI threshold was set at 0. The potential and final LSWI thresholds were identified (Eqs. (3) and (4)).

$$T_P = LSWI_{min} + (LSWI_{max} - LSWI_{min}) \times 0.15 \qquad (3)$$

$$T_F = \begin{cases} 0 \, (T_P < 0) \\ T_P \, (0 \le T_P \le 0.2) \\ 0.2 \, (T_P > 0.2) \end{cases} \qquad (4)$$

where T_P is the potential LSWI threshold, T_F is the final LSWI threshold, and $LSWI_{max}$ and $LSWI_{min}$ are the maximum and minimum LSWI values during the two years, respectively. We used the final LSWI threshold to identify the period of bare soil ($LSWI < T_F$).

Step 3. Because a short rice harvesting–transplanting period can be overlooked, a supplementary algorithm was applied. When NDVI values were between 0.2 and 0.5, the pixels were considered a mixture of bare soil and vegetation. Pixels with NDVI values above 0.5 were considered fully vegetated (Sobrino et al., 2001). Thus, the threshold for the maximum NDVI value during a crop's growth period was set to 0.5. Areas where the maximum NDVI value was < 0.5 were identified as non-cropped, and areas where the NDVI value was larger than 0.5 were not identified as bare soil. When there were two neighboring waves, if the maximum NDVI values of both waves were > 0.5 and the NDVI value of the trough between the two waves was smaller than 0.5 between June and September, then both waves were identified as crop growth cycles (Eq. 5).

$$NDVI_a > 0.5 \; and \; NDVI_b > 0.5 \; and \; NDVI_c < 0.5 \qquad (5)$$

where $NDVI_i$ is the NDVI value at time i, a and b are the peaks of the two waves, respectively, and c is the trough between the two waves.

Step 4. If the maximum NDVI value of the wave was < 0.5, then the wave was not detected as a crop growth cycle. Thus, all crop's growth cycles were identified.

Step 5. The SOS and EOS periods of all crops were identified using the NDVI ratio method (Eq. 6) (White et al., 1997).

$$NDVI_{ratio} = \frac{NDVI - NDVI_{min}}{NDVI_{max} - NDVI_{min}} \qquad (6)$$

where $NDVI_{ratio}$ is the NDVI ratio; NDVI is the NDVI value at a certain time; $NDVI_{min}$ represents the NDVI value of bare soil, which is calculated as the minimum NDVI value over two years; and $NDVI_{max}$ represents the highest NDVI value of crops, which is calculated as the

maximum NDVI value of each crop's growth cycle. We selected NDVI ratio thresholds of 0.1 for SOS and 0.19 for EOS (You et al., 2013).

Step 6. If the SOS or EOS period of the crop was in 2017, then the multiple cropping index (MCI) was defined as 0.5. If all SOS and EOS periods of the crop were in 2017, then MCI was defined as 1 (Fig. 6). The MCI in 2017 was mapped using a summary of MCI values for all crops in 2017.

2.3.3. Regional implementation of algorithms

Cropland data from the National Land Cover Database for China (NLCD-China) datasets (Liu et al., 2014; Ning et al., 2018) for 2015, at a scale of 1:100,000, were used to mask all remote sensing datasets to exclude non-cropland pixels. Using the described algorithm, MCI was identified using crop phenological information. Because the MCI was calculated as 0.5, 1.5, or 2.5, cropping intensity was defined as follows: single cropping, $1 \leq MCI < 2$; double cropping, $2 \leq MCI < 3$; and triple cropping, $MCI \geq 3$. These values were used to generate a cropping intensity map for 2017.

2.4. Accuracy assessment of cropping intensity maps

A stratified random sampling design was used to validate our algorithms and assess their accuracy for mapping cropping intensity. To reduce the standard error of producer accuracy (PA), user accuracy (UA) and overall accuracy (OA) (Olofsson et al., 2014), we allocated samples in each stratum (single, double, or triple cropping) in proportion to the area of the stratum. We randomly selected 100 sample points among each of the seven study areas (Fig. 7) according to the areal proportion for validation, including 469 samples for single cropping, 228 samples for double cropping, and 3 samples for triple cropping (Table 3). Note that the double cropping samples in area A, triple cropping samples in area F and triple cropping samples in area G (1, 1, 2, respectively) were few (1 to 2), which affected the accuracy assessment. Thus, we decided to increase validation numbers to 10 for each of these three cases.

As cropping intensity is calculated using the number of crop growth cycles during a certain period, instantaneous field sampling data cannot be used to reflect cropping intensity. Field surveys were conducted in June 2017 to collect ground data samples for training and validation, focusing mainly on major cropping intensity and crop types in high-standard basic farmland. These field surveys collected 376 photographs and 353 questionnaires covering all study areas (Fig. 7). The photographs recorded representative crop types with geo-referenced information. Questionnaires were sent to local farmers and government managers who have owned or managed the high-standard basic farmlands. The questionnaire included a set of questions including location, crop intensity, main crop types, sown area and irrigation status.

Then we generated 30 m × 30 m square buffers using these random points. We combined the geo-referenced field photographs, questionnaire results, very high-resolution Google Earth images, and VI profiles to visually interpret actual cropping intensity for all sample points. Finally, using the cropping intensity maps and sample data, we calculated confusion matrices for accuracy assessment.

2.5. Comparison with the national statistical data

The sown areas derived from remote sensing data were compared with the national statistical data at the county level for validation. These statistical data were collected from the provincial statistical yearbook or prefectural statistical yearbook for 2018, which provide information on the sown area for each county. Although these data have some problems, the national statistical dataset is the only available source of data regarding cropping intensity. We selected 112 counties for validation (Table 3); 99% of the area of each selected county fell within the 7 study areas and sown area data for 2017 were

available in the statistical yearbook. We estimated the sown area of each county from our cropping intensity data, which were counted twice (three times) for double (triple) cropping.

3. Results

3.1. Accuracy assessment of cropping intensity maps

A confusion matrix was calculated using the validation sample points (Section 2.4) and used to assess the accuracy of the cropping intensity maps (Table 4). The OA was 93% and the Kappa coefficient was 0.83 over all study areas. The single cropping category had UA and PA values of 93% and 96%, respectively; the double cropping category had UA and PA values of 92% and 86%. PA was higher than UA for single cropping detection but lower for double cropping detection. UA and PA were higher for single cropping detection than for double cropping detection.

The accuracy of the cropping intensity maps differed among study areas, with an OA of 88–99% and a Kappa coefficient of 0.75–0.91. All cropping intensity maps were reasonably accurate, indicating that the cropping intensity identification algorithms were generally reliable when supplemented with of Sentinel-2 imagery. Region A had the highest accuracy (OA: 99%), followed by region B (OA: 96%, Kappa: 0.91), while region F (OA: 88%, Kappa: 0.75) and region G (OA: 88%, Kappa: 0.76) had lower accuracies. Generally, the accuracy of cropping intensity in northern China was significantly higher than those in southern China. The main reason for this difference was that there were more high-quality images from northern China than from southern China. Furthermore, southern China has more complex cropping-intensity and crop-type patterns compared to northern China, which might also have affected map accuracy. This possibility is supported by the accuracy in areas where single cropping dominated being higher than that in areas of complex cropping intensity. Identification of single cropping using this algorithm requires high-quality observations in only three periods (before sowing, after harvest and during the maturation period of crops), each of which lasts a relatively long time. Double cropping and triple cropping necessitate high-quality observations in more periods: as well as the three periods mentioned above, observations are needed from between the harvest of early crops and the sowing of later crops. Moreover, for double cropping and triple cropping, the duration of each of these periods is relatively short compared to the duration of the three periods for single cropping.

3.2. Comparison of cropping intensity maps with national statistical data

We compared the cropping intensity maps with the national statistical data for 2017 at the county level. The sown areas obtained from the cropping intensity maps and the national statistical data at the county level had a significant linear relationship, with R^2 of 0.82 (Fig. 8). Mean error (ME) and root mean square error (RMSE) are two statistical measures that can be used to compare two datasets. The ME was 24,351 ha and RMSE was 38,569 ha for all seven study areas (Table 5). The sown area was greater in the cropping intensity maps than in the national statistical data for all study areas, mainly because the cropland area was larger in NLCD-China than in the national statistical yearbook. The results of accuracy assessment indicated that region A had the strongest correlation (RMSE: 32,519 ha, ME: 20,645 ha), followed by region B (RMSE: 34,295 ha, ME: 22,495 ha), whereas region F (RMSE: 43,970 ha, ME: 14,807 ha) and region G (RMSE: 46,131 ha, ME: 36,691 ha) had weaker correlations. The correlation was much stronger for northern China than for southern China.
C

3.3. Maps of cropping intensity in 2017

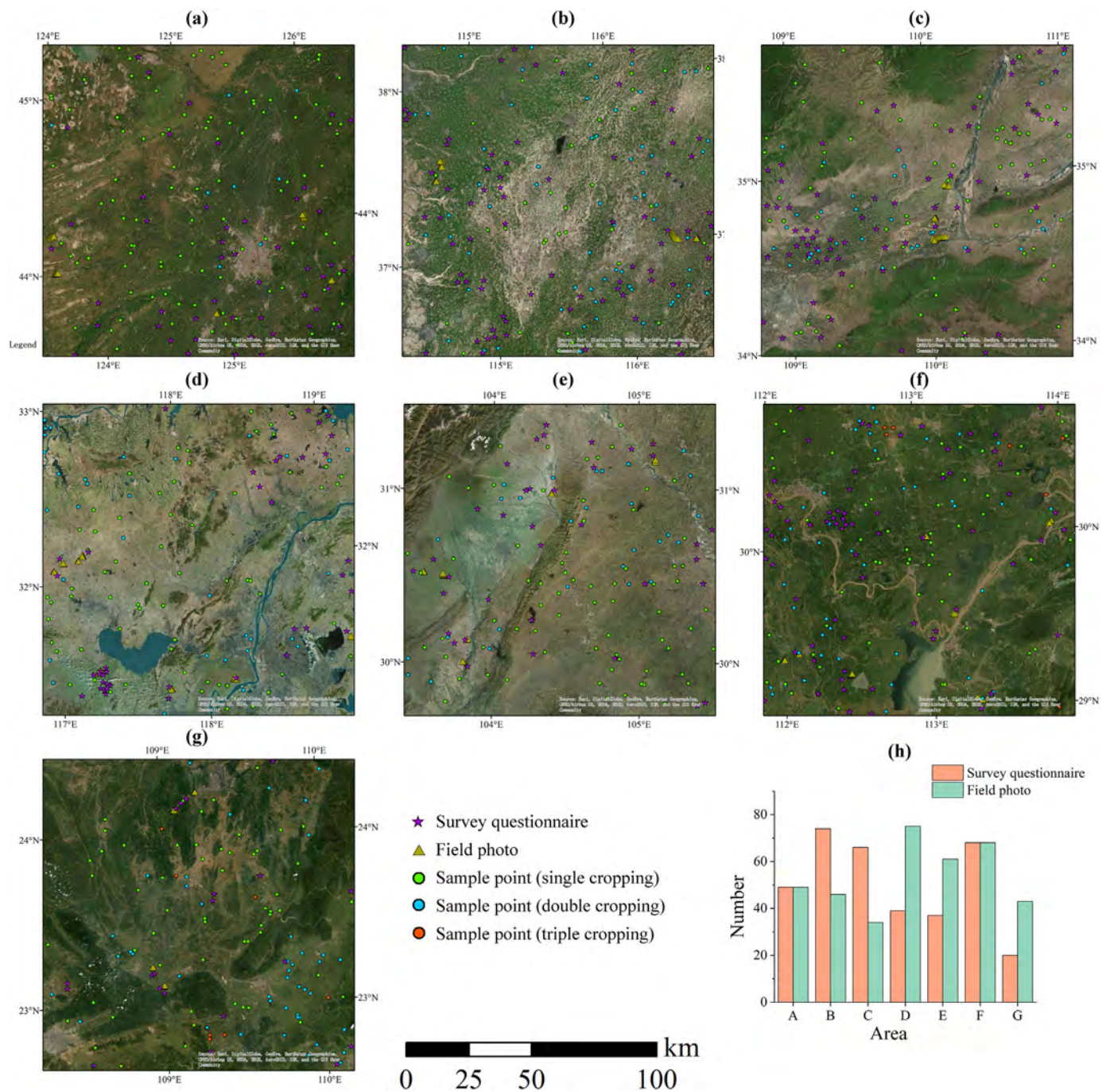We mapped cropping intensity in 2017 at 30 m spatial resolution

Fig. 7. (a - g) Spatial distributions of validation points in each study area (A – G, respectively). (h) Numbers of survey questionnaires and field photos collected in all study areas.

Table 3
Numbers of sampling points and counties used for validation in each study area.

		A	B	C	D	E	F	G	Total
Sampling point	Single cropping	99	33	72	65	77	65	58	469
	Double cropping	1[a]	67	28	35	23	34	40	228
	Triple cropping	0	0	0	0	0	1[a]	2[a]	3
County		4	42	19	15	13	11	8	112

[a] Number increased to 10.

using the algorithms described in Section 2.3. Fig. 9 shows the resulting cropping intensity maps for each of the seven study areas. The spatial distribution of cropping intensity was consistent with climate factors

and topographical characteristics.

In Region A, cropping intensity was dominated by single cropping of crops such as maize, soybean or paddy rice due to the relatively cold weather in winter. Double cropping was also detected in extremely small areas due to double vegetable planting. In Regions B and C, double cropping is widely applied by planting winter wheat and maize. However, the local government has promoted a "one cropping for fallow, one cropping for rainfed" policy since 2014 due to a lack of groundwater and rainfall in winter around Hengshui City in Region B; therefore, farmers have abandoned double cropping and adopted single cropping for soybean, cotton, peanut, oil sunflower, and other grains. Maize is planted only at great distances from the Wei and Yellow Rivers mainly due to a lack of water for irrigation in Region C. Thus, single

Table 4
Accuracy assessment of cropping intensity in each study area. A – Northeast China Plain, B – North China Plain, C – Guanzhong Plain, D – Tai Lake Plain, E – Sichuan Basin, F – Dongting Lake Plain, G – Central Guangxi Plain.

| Region	Cropping intensity	User accuracy	Producer accuracy	Overall accuracy	Kappa coefficient
A	Single	100%	99%	99%	–
	Double	80%	–		
	Triple	–	–		
B	Single	97%	91%	96%	0.91
	Double	96%	98%		
	Triple	–	–		
C	Single	94%	97%	94%	0.85
	Double	93%	87%		
	Triple	–	–		
D	Single	94%	94%	92%	0.82
	Double	89%	89%		
	Triple	–	–		
E	Single	91%	97%	91%	0.76
	Double	91%	75%		
	Triple	–	–		
F	Single	86%	97%	89%	0.77
	Double	94%	78%		
	Triple	80%	–		
G	Single	90%	91%	89%	0.77
	Double	88%	85%		
	Triple	80%	100%		
Total	Single	93%	96%	93%	0.84
	Double	92%	87%		
	Triple	80%	100%		
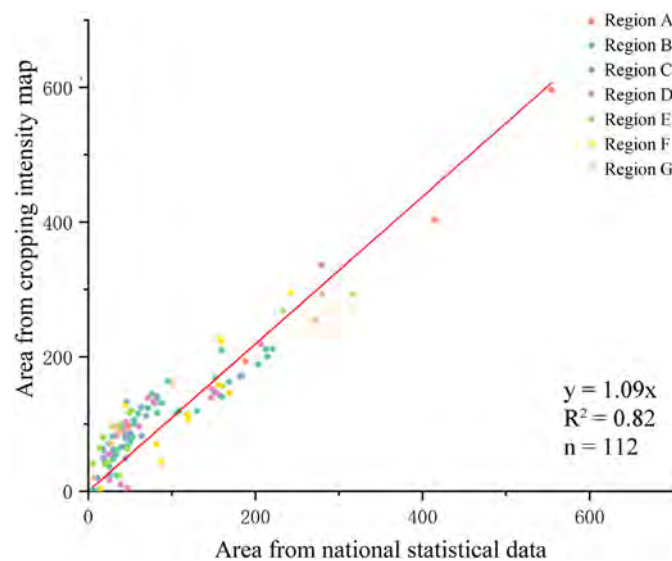
Fig. 8. Comparison of sown area (thousand ha) obtained from cropping intensity maps with area obtained from national statistical data.

Table 5
Comparison of sown area (ha) derived from cropping-intensity maps and sown area derived from national statistical data.

	A	B	C	D	E	F	G	Total
ME	20,645	22,495	28,242	21,033	30,113	14,807	36,691	24,351
RMSE	32,519	34,295	37,817	39,856	42,690	43,970	46,131	38,569

cropping was also detected in Regions B and C.

In Regions D and F, due to warm climate and abundant rainfall, two seasons of paddy rice or winter rapeseed–rice systems are generally adopted per year for double cropping. However, only one season of rice was planted per year during the study period due to a lack of rural labor in economically developed regions, leading to the detection of single

cropping. In region E, due to varied topography and water availability, there was a complex pattern of multiple cropping systems. In Chengdu Plain, in the western part of region E, winter rape–rice or winter wheat–maize are widely adopted for double cropping. By contrast, one season of rice or maize per year is planted for single cropping in the hilly eastern part of Region E. In Region G, single cropping was identified in areas where fruit, sugarcane, and cassava were planted, whereas double or triple cropping was detected in areas planting rice, maize, and vegetables.

4. Discussion

4.1. Integration of times series Landsat and Sentinel-2 imagery

The algorithm used to identify cropping intensity in previous studies have mainly been based on moderate-resolution images (i.e., MODIS products) (Biradar and Xiao, 2011; Gray et al., 2014; Li et al., 2014; Liu et al., 2012; Xiao et al., 2006; Xiao et al., 2005; Yan et al., 2014). However, the accuracy of data products based on these algorithms is limited due to high sub-pixel heterogeneity (Jain et al., 2013). For example, the cropland area own by 90% of farmers in China is < 0.2 ha (Li et al., 2006). One study found that field size is very small in most areas of southern and eastern China (Fritz et al., 2015). In particular, cropping systems in southern China are characterized by smallholder farms, and the field size of most croplands is < 0.04 ha, although many croplands have been reclaimed over the past 10 years (Tan et al., 2013). Thus, the 500-m resolution of MODIS is clearly insufficient (Ozdogan and Woodcock, 2006; Podwysocki, 1976).

Both Landsat and Sentinel-2 provide high spatial resolution images (10–30 m) at sixteen days and six days temporal resolution. (Zhang et al., 2018). Integration of Landsat and Sentinel-2 data greatly increase (at least twofold) the temporal frequency of good-quality observations (Li and Roy, 2017), providing an opportunity to generate high-resolution cropping intensity maps based on phenology analysis (Griffiths et al., 2019; Wang et al., 2019; Zhong et al., 2019). Such an improvement allows high-resolution crop type mapping and agricultural monitoring by tracking crop phenology.

We compared annual maps of cropping intensity identified by Landsat, Sentinel-2, and integrated Landsat and Sentinel-2 images (Table 6). The cropping intensity map generated by the integration of Landsat and Sentinel-2 data had high OA (93%) and Kappa coefficient (0.83) values, whereas cropping intensity maps generated from Landsat or Sentinel-2 data had lower OA values (76% and 78%, respectively) and Kappa coefficients (0.46 and 0.50, respectively). Notably, 5% of sample points could not be identified as crops based on Landsat images alone due to a lack of sufficient good-quality observations. In particular, cropping intensity maps from southern China based on Landsat (in regions F and G) or Sentinel-2 (in regions D and E) data had unacceptably low accuracy. Comparatively, cropping-intensity maps based on integrated Landsat and Sentinel-2 images had relatively high accuracy. Thus, cropping-intensity maps created by integrating Landsat and Sentinel-2 images had greatly improved accuracy. This improved accuracy resulted from the greater number of high-quality observations available, which provided more phenological information about crops for extraction of cropping intensity. We obtained 67–168 high-quality observations from the integration of Landsat and Sentinel-2 data during the study period, compared to 25–67 and 39–101 high-quality observations from Landsat and Sentinel-2, respectively (Fig. 2).

4.2. Algorithm development and critical conditions

Peak counting algorithms have been used to map cropping intensity in previous studies (Heller et al., 2012; Qiu et al., 2017; Yan et al., 2018a). However, some crops tend to manifest two NDVI (or EVI) peaks for each seasonal crop. For example, winter wheat has two similar peaks and cycles (Fig. 10a, November 2017 to May 2018). The NDVI
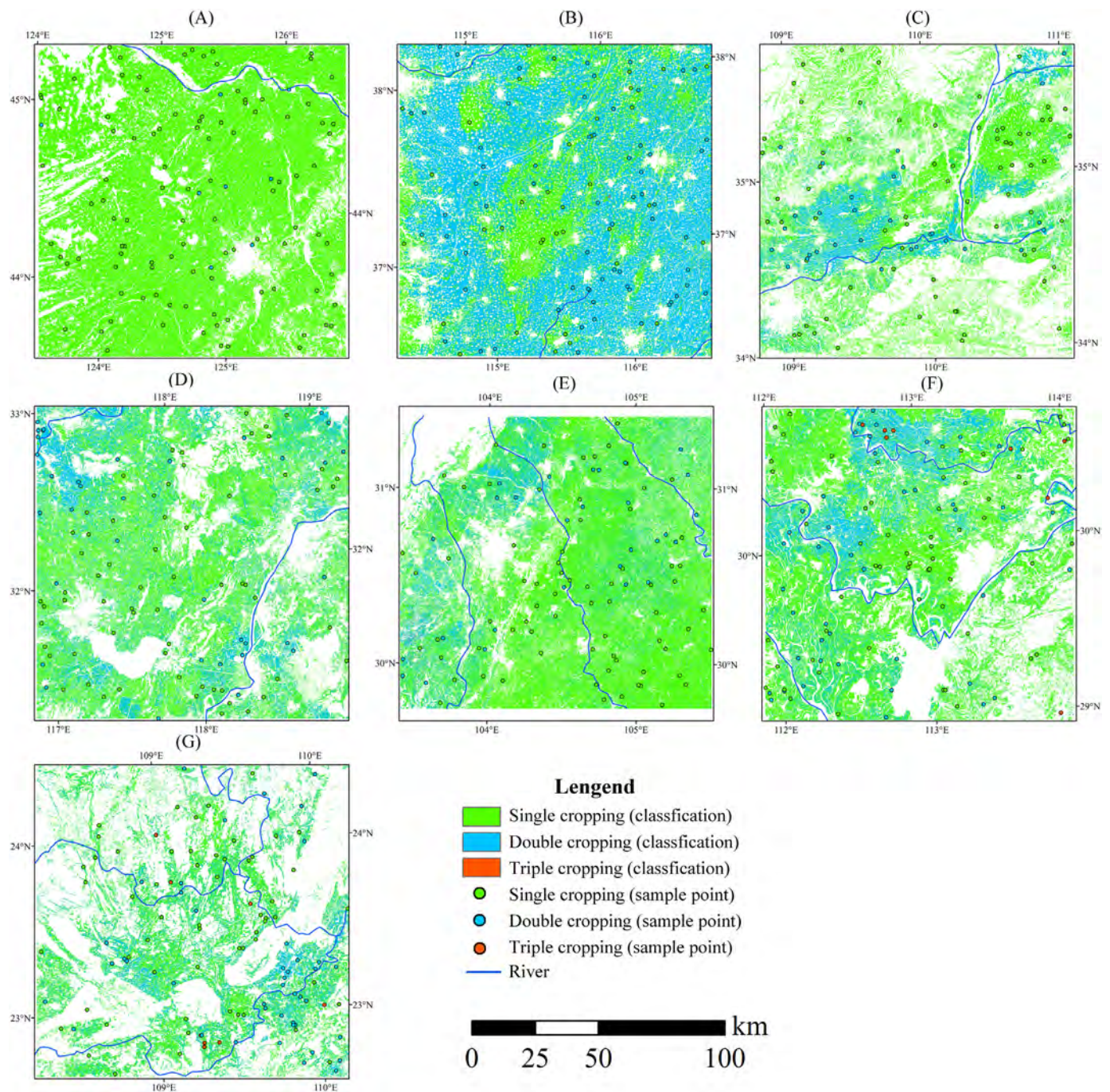
Fig. 9. Spatial distribution of cropping intensity in each study zone (A - G). Blank areas represent non-cropland areas that were masked in the cropland dataset and were not classified in this study.

values of both peaks are relatively high (> 0.6), and both cycles are longer than 90 days. Therefore, it is difficult to identify crop growth cycles using only the NDVI temporal profile (Gray et al., 2014). Some studies have used the calendar-year thermal growth season to exclude the additional winter crop peak by avoiding the identification of autumn growth of the winter crop as a separate crop cycle (Gray et al., 2014). However, some summer crops (e.g., sugarcane) also have multiple peaks in each seasonal crop (Fig. 10b, April to October 2017), due to the impact of bad climate conditions on crop growth and image quality.

In this study, crop growth cycles were identified based on the simple principle that bare soil and/or dead vegetation, which can be identified by LSWI values, must exist before sowing and after harvesting. Our

algorithm successfully mapped cropping intensity at large scales across China. However, LSWI values were calculated using images from optical sensors, which are affected by cloud and shadow (Zhu et al., 2015). The accuracy of the algorithm will decrease if no good-quality observations are available for identification of bare soil, due to cloud or shadow. Because microwave images from Sentinel-1 can easily pass through clouds (Periasamy, 2018), Sentinel-1 data can be used to identify bare soil instead of LSWI data, based on the degree of depolarization attained by the illuminated signal at the incident plane (Periasamy, 2018; Vreugdenhil et al., 2018), further improving results even during periods of high cloud cover by integrating optical and radar sensors (Bargiel, 2017; Van Tricht et al., 2018; Veloso et al., 2017).

Table 6
Accuracy assessment of cropping intensity identified using imagery from Landsat, Sentinel-2, and integration of Landsat and Sentinel-2.

Region	Landsat		Sentinel-2		Landsat and Sentinel-2	
	Overall accuracy	Kappa coefficient	Overall accuracy	Kappa coefficient	Overall accuracy	Kappa coefficient
A	98%	–	99%	–	99%	–
B	85%	0.69	89%	0.77	96%	0.91
C	71%	0.36	76%	0.49	94%	0.85
D	79%	0.57	67%	0.26	92%	0.82
E	78%	0.43	69%	0.17	91%	0.76
F	64%	0.20	77%	0.51	89%	0.77
G	59%	0.13	68%	0.35	89%	0.77
Total	76%	0.46	78%	0.50	93%	0.84

4.3. Potential sources of uncertainty

Several factors may affect the accuracy of cropping intensity maps derived from the proposed algorithms. First, we used the NLCD-China datasets, which are widely used land cover datasets for China (Ning et al., 2018), to distinguish croplands from other land cover types; the data source clearly affects the accuracy of the resultant cropping intensity maps. However, the spatial resolution of the NLCD-China dataset (100 m) is coarser than the 30-m spatial resolution of the resultant cropping intensity maps, which may increase the error of our results (Ozdogan and Woodcock, 2006). Second, to exclude grass and shrubs before planting or after harvest, our algorithm requires that the maximum NDVI value of each cycle exceeds 0.5. Vegetation can interfere with crop identification, because the maximum NDVI value of the vegetation cycle may be similar to that of crops (> 0.6) or shrubs (< 0.4) due to differences in vegetation types and climate factors (Teluguntla et al., 2018). The maximum NDVI value of the crop cycle may be < 0.5 in poor-quality images. Finally, there were incorrect results among some "salt and pepper" pixels in comparisons between fields or between field and non-cropland, particularly in hilly areas, due to noise in the mixed pixel time series, resulting in errors. We also detected mismatches of pixel dimensions across time among the Sentinel-2 data (Yan et al., 2018b). An object-based identification algorithm for Sentinel-2 Level-2A data may alleviate these problems (Belgiu and Csillik, 2018; Pena-Barragan et al., 2011; Xiong et al., 2017a).

4.4. Advantages of the Google Earth Engine

The GEE is a cloud-based geospatial analysis platform that includes very large databases, immense computational power, and numerous algorithms. The GEE facilitates processing large numbers of high-resolution images for mapping crop intensity. The GEE provides different levels of processed imagery products (analysis-ready datasets) in timely fashion for direct use. Its high-performance computing and parallel-processing platform can be used to process large-scale geospatial datasets. The GEE requires only 40 min to identify cropping intensity within an area of 200 km × 200 km from approximately 4 TB of images. On the other hand, the GEE cannot process extremely complex algorithms, which would exceed memory limits.

4.5. Implications and future work

Cropland is the most complex land use type as it is affected by both human activity and the natural environment. Annual cropping intensity maps can be used to elucidate the impacts of cropland on regional climate, biogeochemical cycles (e.g., carbon, nitrogen, and greenhouse gases), and water resources (Biradar and Xiao, 2011). Cropping intensity has undergone extensive changes throughout China due to climate change and land policy changes (Yan et al., 2018a), as approaches to increase food production are sought (Wu et al., 2014; Zhang et al., 2014). Comparison of actual and potential cropping intensity can help farmers to improve crop planting decisions and policy makers to make science-based policies to increase food production in food-insecure regions (Wu et al., 2018). In future studies, we will apply these algorithms extensively to map annual cropping intensity spatially and temporally throughout China.

Mapping crop types has typically involved the use of all available images to identify characteristic information for each crop (Griffiths et al., 2019; Massey et al., 2017; Wang et al., 2019; Zhong et al., 2011). However, information from the non-growth period interferes with the extraction of desired crop information. Crop type identification is also affected by data for other crops within multiple cropping systems. The algorithms proposed in this study successfully extracted growth cycle information for each crop, which was then used to map crop types by identifying crop characteristics within their specific growth cycles. Phenological information was also extracted throughout the crop growth cycle, and images of the key phenology periods were selected to identify each crop type.

5. Conclusion

We developed and implemented a pixel- and phenology-based algorithm for mapping cropping intensity, defined as the number of crop growth cycles within a specified time period, using integrated time series data acquired by Landsat and Sentinel-2. The algorithm was applied to cropland across China. The NDVI time series dataset was obtained from combined Landsat and Sentinel-2 imagery, and was then gap-filled and smoothed using a linear interpolation method and adaptive Savitzky–Golay filter, respectively. Bare soil information was detected using LSWI values and used to identify crop growth cycles. The
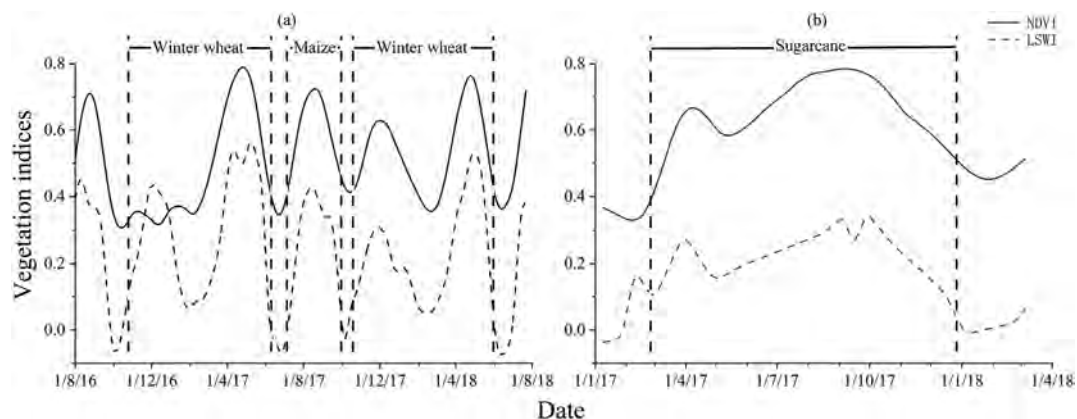

Fig. 10. Temporal profile of vegetation indices (NDVI and LSWI) for winter wheat (114.8723°E, 37.4842°N) (a) and sugarcane (108.6083°E, 24.2099°N) (b).

OA of the resultant maps was 93% and the Kappa coefficient was 0.83 over all seven study areas. High-accuracy annual cropping intensity maps, with a spatial resolution of 30 m, were generated by counting detected crop growth cycles. Compared to cropping intensity maps based on images with coarse spatial resolution, such as those from MODIS, the 30-m cropping intensity map exhibited greatly reduced mixed-pixel effects, more detailed spatial distribution, and greatly improved accuracy, particularly for smallholder farms. Although this algorithm was tested in only seven study areas within major grain-producing regions in China, it could be applied throughout China and in other countries where multiple cropping systems are implemented. The algorithm could also be applied to quantify inter-annual cropping intensity variation.

Authors contribution

Luo Liu: Conceptualization, Methodology, Writing; **Xiangming Xiao:** Supervision, Project administration; **Yuanwei Qin:** Conceptualization; **Jie Wang:** Methodology; **Xinliang Xu:** Validation; **Yueming Hu:** Project administration; **Zhi Qiao:** Validation.

Declaration of competing interests

The authors declare that they have no known competing financial interests or personal relationships that could have appeared to influence the work reported in this paper.

Acknowledgements

References

Arvidson, T., Goward, S., Gasch, J., Williams, D., 2006. Landsat-7 long-term acquisition plan. Photogramm. Eng. Remote Sens. 72, 1137–1146.

Bargiel, D., 2017. A new method for crop classification combining time series of radar images and crop phenology information. Remote Sens. Environ. 198, 369–383.

Becker-Reshef, I., Vermote, E., Lindeman, M., Justice, C., 2010. A generalized regression-based model for forecasting winter wheat yields in Kansas and Ukraine using MODIS data. Remote Sens. Environ. 114, 1312–1323.

Belcher, K.W., Boehm, M.M., Fulton, M.E., 2004. Agroecosystem sustainability: a system simulation model approach. Agric. Syst. 79, 225–241.

Belgiu, M., Csillik, O., 2018. Sentinel-2 cropland mapping using pixel-based and object-based time-weighted dynamic time warping analysis. Remote Sens. Environ. 204, 509–523.

Biradar, C.M., Xiao, X.M., 2011. Quantifying the area and spatial distribution of double- and triple-cropping croplands in India with multi-temporal MODIS imagery in 2005. Int. J. Remote Sens. 32, 367–386.

Boles, S.H., Xiao, X., Liu, J., Zhang, Q., Munkhtuya, S., Chen, S., Ojima, D., 2004. Land cover characterization of temperate East Asia using multi-temporal VEGETATION sensor data. Remote Sens. Environ. 90, 477–489.

Chen, B., Xiao, X., Ye, H., Ma, J., Doughty, R., Li, X., Zhao, B., Wu, Z., Sun, R., Dong, J., 2018. Mapping forest and their spatial–temporal changes from 2007 to 2015 in tropical Hainan island by integrating ALOS/ALOS-2 L-band SAR and landsat optical images. IEEE Journal of Selected Topics in Applied Earth Observations and Remote Sensing 11, 852–867.

Dietrich, J.P., Schmitz, C., Müller, C., Fader, M., Lotze-Campen, H., Popp, A., 2012. Measuring agricultural land-use intensity–a global analysis using a model-assisted approach. Ecol. Model. 232, 109–118.

Dong, J., Xiao, X., Kou, W., Qin, Y., Zhang, G., Li, L., Jin, C., Zhou, Y., Wang, J., Biradar, C., 2015. Tracking the dynamics of paddy rice planting area in 1986–2010 through time series Landsat images and phenology-based algorithms. Remote Sens. Environ. 160, 99–113.

Fan, C., Zheng, B., Myint, S.W., Aggarwal, R., 2014. Characterizing changes in cropping patterns using sequential Landsat imagery: an adaptive threshold approach and application to Phoenix, Arizona. Int. J. Remote Sens. 35, 7263–7278.

Fischer, G., Van Velthuizen, H., Shah, M., Nachtergaele, F., 2002. Global Agro-Ecological Assessment for Agriculture in the 21st Century: Methodology and Results. International Institute for Applied Systems Analysis.

Foga, S., Scaramuzza, P.L., Guo, S., Zhu, Z., Dilley, R.D., Beckmann, T., Schmidt, G.L., Dwyer, J.L., Hughes, M.J., Laue, B., 2017. Cloud detection algorithm comparison and validation for operational Landsat data products. Remote Sens. Environ. 194, 379–390.

Fritz, S., See, L., McCallum, I., You, L., Bun, A., Moltchanova, E., Duerauer, M., Albrecht, F., Schill, C., Perger, C.J.G., 2015. Mapping Global Cropland and Field Size. 21. pp. 1980–1992.

Galford, G.L., Mustard, J.F., Melillo, J., Gendrin, A., Cerri, C.C., Cerri, C.E.P., 2008. Wavelet analysis of MODIS time series to detect expansion and intensification of row-crop agriculture in Brazil. Remote Sens. Environ. 112, 576–587.

Gorelick, N., Hancher, M., Dixon, M., Ilyushchenko, S., Thau, D., Moore, R., 2017. Google earth engine: planetary-scale geospatial analysis for everyone. Remote Sens. Environ. 202, 18–27.

Gray, J., Friedl, M., Frolking, S., Ramankutty, N., Nelson, A., Gumma, M.K., 2014. Mapping Asian cropping intensity with MODIS. IEEE Journal of Selected Topics in Applied Earth Observations and Remote Sensing 7, 3373–3379.

Griffiths, P., Nendel, C., Hostert, P., 2019. Intra-annual reflectance composites from Sentinel-2 and Landsat for national-scale crop and land cover mapping. Remote Sens. Environ. 220, 135–151.

Guo, W., 1986. The historical development of China's multiple cropping system. World Agriculture 39–42.

Heller, E., Rhemtulla, J.M., Lele, S., Kalacska, M., Badiger, S., Sengupta, R., Ramankutty, N., 2012. Mapping crop types, irrigated areas, and cropping intensities in heterogeneous landscapes of Southern India using multi-temporal medium-resolution imagery: implications for assessing water use in agriculture. Photogramm. Eng. Remote. Sens. 78, 815–827.

Iizumi, T., Ramankutty, N., 2015. How do weather and climate influence cropping area and intensity? Global Food Security 4, 46–50.

Jain, M., Mondal, P., DeFries, R.S., Small, C., Galford, G.L., 2013. Mapping cropping intensity of smallholder farms: a comparison of methods using multiple sensors. Remote Sens. Environ. 134, 210–223.

Kandasamy, S., Baret, F., Verger, A., Neveux, P., Weiss, M., 2013. A comparison of methods for smoothing and gap filling time series of remote sensing observations–application to MODIS LAI products. Biogeosciences 10, 4055–4071.

Lenney, M.P., Woodcock, C.E., Collins, J.B., Hamdi, H., 1996. The status of agricultural lands in Egypt: the use of multitemporal NDVI features derived from Landsat TM. Remote Sens. Environ. 56, 8–20.

Li, J., Roy, D., 2017. A global analysis of Sentinel-2A, Sentinel-2B and Landsat-8 data revisit intervals and implications for terrestrial monitoring. Remote Sens. 9, 902.

Li, J.C., Yuqi, Zhang, Q., Kuang, X., 2006. Reasons and countermeasures of cropland fragmentation in China. Agric. Econ. 6, 21–23.

Li, L., Friedl, M.A., Xin, Q.C., Gray, J., Pan, Y.Z., Frolking, S., 2014. Mapping crop cycles in China using MODIS-EVI time series. Remote Sens. 6, 2473–2493.

Liu, J., Liu, M., Tian, H., Zhuang, D., Zhang, Z., Zhang, W., Tang, X., Deng, X.J.R., 2005. Spatial and Temporal Patterns of China's Cropland during 1990–2000: An Analysis Based on Landsat TM Data. 98. pp. 442–456.

Liu, J., Zhu, W., Cui, X., 2012. A shape-matching cropping index (CI) mapping method to determine agricultural cropland intensities in China using MODIS time-series data. Photogramm. Eng. Remote Sens. 78, 829–837.

Liu, L., Xu, X., Zhuang, D., Chen, X., Li, S., 2013. Changes in the potential multiple cropping system in response to climate change in China from 1960–2010. PLoS One 8, e80990.

Liu, J.Y., Kuang, W.H., Zhang, Z.X., Xu, X.L., Qin, Y.W., Ning, J., Zhou, W.C., Zhang, S.W., Li, R.D., Yan, C.Z., Wu, S.X., Shi, X.Z., Jiang, N., Yu, D.S., Pan, X.Z., Chi, W.F., 2014. Spatiotemporal characteristics, patterns, and causes of land-use changes in China since the late 1980s. J. Geogr. Sci. 24, 195–210.

Massey, R., Sankey, T.T., Congalton, R.G., Yadav, K., Thenkabail, P.S., Ozdogan, M., Meador, A.J.S., 2017. MODIS phenology-derived, multi-year distribution of conterminous US crop types. Remote Sens. Environ. 198, 490–503.

Meylan, L., Merot, A., Gary, C., Rapidel, B., 2013. Combining a typology and a conceptual model of cropping system to explore the diversity of relationships between ecosystem services: the case of erosion control in coffee-based agroforestry systems in Costa Rica. Agric. Syst. 118, 52–64.

Ning, J., Liu, J., Kuang, W., Xu, X., Zhang, S., Yan, C., Li, R., Wu, S., Hu, Y., Du, G.J.J.S., 2018. Spatiotemporal Patterns and Characteristics of Land-Use Change in China during 2010–2015. 28. pp. 547–562.

Olofsson, P., Foody, G.M., Herold, M., Stehman, S.V., Woodcock, C.E., Wulder, M.A., 2014. Good practices for estimating area and assessing accuracy of land change. Remote Sens. Environ. 148, 42–57.

Ozdogan, M., Woodcock, C.E., 2006. Resolution dependent errors in remote sensing of cultivated areas. Remote Sens. Environ. 103, 203–217.

Pena-Barragan, J.M., Ngugi, M.K., Plant, R.E., Six, J., 2011. Object-based crop identification using multiple vegetation indices, textural features and crop phenology. Remote Sens. Environ. 115, 1301–1316.

Periasamy, S., 2018. Significance of dual polarimetric synthetic aperture radar in biomass retrieval: an attempt on Sentinel-1. Remote Sens. Environ. 217, 537–549.

Podwysocki, M.H., 1976. Analysis of Field Size Distributions, LACIE Test Sites 5029, 5033, and 5039, Anhwei Province, People's Republic of China.

Qiu, B., Lu, D., Tang, Z., Song, D., Zeng, Y., Wang, Z., Chen, C., Chen, N., Huang, H., Xu, W.J.A., 2017. Mapping Cropping Intensity Trends in China during 1982–2013. 79. pp. 212–222.

Quarmby, N.A., Townshend, J.R.G., Settle, J.J., White, K.H., Milnes, M., Hindle, T.L., Silleos, N., 1992. Linear mixture modeling applied to Avhrr data for crop area estimation. Int. J. Remote Sens. 13, 415–425.

Roy, D.P., Kovalskyy, V., Zhang, H.K., Vermote, E.F., Yan, L., Kumar, S.S., Egorov, A., 2016. Characterization of Landsat-7 to Landsat-8 reflective wavelength and normalized difference vegetation index continuity. Remote Sens. Environ. 185, 57–70.

Running, S.W., Loveland, T.R., Pierce, L.L., Nemani, R., Hunt, E.R., 1995. A remote-sensing based vegetation classification logic for global land-cover analysis. Remote

Sens. Environ. 51, 39–48.

Sakamoto, T., Yokozawa, M., Toritani, H., Shibayama, M., Ishitsuka, N., Ohno, H., 2005. A crop phenology detection method using time-series MODIS data. Remote Sens. Environ. 96, 366–374.

Sobrino, J., Raissouni, N., Li, Z.-L.J.R.S., 2001. A Comparative Study of Land Surface Emissivity Retrieval from NOAA Data. 75. pp. 256–266.

Tan, M., Robinson, G.M., Li, X., Xin, L.J.C.g.s., 2013. Spatial and temporal variability of farm size in China in context of rapid urbanization. 23, 607–619.

Teluguntla, P., Thenkabail, P., Oliphant, A., Xiong, J., Gumma, M.K., Congalton, R.G., Yadav, K., Huete, A., 2018. A 30-m landsat-derived cropland extent product of Australia and China using random forest machine learning algorithm on Google Earth Engine cloud computing platform. ISPRS J. Photogramm. Remote Sens. 144, 325–340.

Tucker, C.J., 1979. Red and photographic infrared linear combinations for monitoring vegetation. Remote Sens. Environ. 8, 127–150.

USDA, 1994. Major world crop areas and climatic profiles. In: Agricultural Handbook No. 664, pp. 279.

Van Tricht, K., Gobin, A., Gilliams, S., Piccard, I., 2018. Synergistic use of radar Sentinel-1 and optical Sentinel-2 imagery for crop mapping: a case study for Belgium. Remote Sens. 10, 1642.

Van Wart, J., van Bussel, L.G., Wolf, J., Licker, R., Grassini, P., Nelson, A., Boogaard, H., Gerber, J., Mueller, N.D., Claessens, L.J.F., 2013. Use of Agro-Climatic Zones to Upscale Simulated Crop Yield Potential. 143. pp. 44–55.

Veloso, A., Mermoz, S., Bouvet, A., Toan, T.L., Planells, M., Dejoux, J.F., Ceschia, E., 2017. Understanding the temporal behavior of crops using Sentinel-1 and Sentinel-2-like data for agricultural applications. Remote Sens. Environ. 199, 415–426.

Vreugdenhil, M., Wagner, W., Bauer-Marschallinger, B., Pfeil, I., Teubner, I., Rüdiger, C., Strauss, P., 2018. Sensitivity of Sentinel-1 backscatter to vegetation dynamics: an Austrian case study. Remote Sens. 10, 1396.

Wang, S., Azzari, G., Lobell, D.B., 2019. Crop type mapping without field-level labels: random forest transfer and unsupervised clustering techniques. Remote Sens. Environ. 222, 303–317.

Wardlow, B.D., Egbert, S.L., Kastens, J.H., 2007. Analysis of time-series MODIS 250 m vegetation index data for crop classification in the US central Great Plains. Remote Sens. Environ. 108, 290–310.

White, M.A., Thornton, P.E., Running, S.W., 1997. A continental phenology model for monitoring vegetation responses to interannual climatic variability. Glob. Biogeochem. Cycles 11, 217–234.

Wu, W., Yu, Q., Peter, V.H., YOU, L., Peng, Y., Tang, H., 2014. How could agricultural land systems contribute to raise food production under global change? J. Integr. Agric. 13, 1432–1442.

Wu, W.B., Yu, Q.Y., You, L.Z., Chen, K., Tang, H.J., Liu, J.G., 2018. Global cropping intensity gaps: increasing food production without cropland expansion. Land Use Policy 76, 515–525.

Xiao, X.M., Boles, S., Liu, J.Y., Zhuang, D.F., Frolking, S., Li, C.S., Salas, W., Moore, B., 2005. Mapping paddy rice agriculture in southern China using multi-temporal MODIS images. Remote Sens. Environ. 95, 480–492.

Xiao, X.M., Boles, S., Frolking, S., Li, C.S., Babu, J.Y., Salas, W., Moore, B., 2006. Mapping paddy rice agriculture in South and Southeast Asia using multi-temporal MODIS images. Remote Sens. Environ. 100, 95–113.

Xiong, J., Thenkabail, P., Tilton, J., Gumma, M., Teluguntla, P., Oliphant, A., Congalton, R., Yadav, K., Gorelick, N., 2017a. Nominal 30-m cropland extent map of continental Africa by integrating pixel-based and object-based algorithms using Sentinel-2 and Landsat-8 data on Google earth engine. Remote Sens. 9, 1065.

Xiong, J., Thenkabail, P.S., Gumma, M.K., Teluguntla, P., Poehnelt, J., Congalton, R.G., Yadav, K., Thau, D., 2017b. Automated cropland mapping of continental Africa using Google Earth Engine cloud computing. ISPRS J. Photogramm. Remote Sens. 126, 225–244.

Yan, H.M., Xiao, X.M., Huang, H.Q., Liu, J.Y., Chen, J.Q., Bai, X.H., 2014. Multiple cropping intensity in China derived from agro-meteorological observations and MODIS data. Chin. Geogr. Sci. 24, 205–219.

Yan, H., Liu, F., Qin, Y., Niu, Z., Doughty, R., Xiao, X., 2018a. Tracking the spatio-temporal change of cropping intensity in China during 2000-2015. Environ. Res. Lett. 14 (3), 15. https://doi.org/10.1088/1748-9326/aaf9c7.

Yan, L., Roy, D., Li, Z., Zhang, H., Huang, H.J.R., 2018b. Sentinel-2A Multi-Temporal Misregistration Characterization and an Orbit-Based Sub-Pixel Registration Methodology. 215. pp. 495–506.

You, X., Meng, J., Zhang, M., Dong, T., 2013. Remote sensing based detection of crop phenology for agricultural zones in China using a new threshold method. Remote Sens. 5, 3190–3211.

Zhang, J., Feng, L., Yao, F., 2014. Improved maize cultivated area estimation over a large scale combining MODIS–EVI time series data and crop phenological information. ISPRS J. Photogramm. Remote Sens. 94, 102–113.

Zhang, H.K.K., Roy, D.P., Yan, L., Li, Z.B., Huang, H.Y., Vermote, E., Skakun, S., Roger, J.C., 2018. Characterization of sentinel-2A and Landsat-8 top of atmosphere, surface, and nadir BRDF adjusted reflectance and NDVI differences. Remote Sens. Environ. 215, 482–494.

Zhong, L.H., Hawkins, T., Biging, G., Gong, P., 2011. A phenology-based approach to map crop types in the San Joaquin Valley, California. Int. J. Remote Sens. 32, 7777–7804.

Zhong, L., Hu, L., Zhou, H., 2019. Deep learning based multi-temporal crop classification. Remote Sens. Environ. 221, 430–443.

Zhu, Z., Woodcock, C.E., 2014. Continuous change detection and classification of land cover using all available Landsat data. Remote Sens. Environ. 144, 152–171.

Zhu, Z., Wang, S., Woodcock, C.E., 2015. Improvement and expansion of the Fmask algorithm: cloud, cloud shadow, and snow detection for Landsats 4–7, 8, and sentinel 2 images. Remote Sens. Environ. 159, 269–277.

Zuo, H., 1996. Agro-Climatic Analysis for Mainland East Asia by a GIS Approach. Australian National University, pp. 264.